

EFFECT OF INTAKE AERODYNAMICS AND FLOW DISTORTION ON FAN STALL INCEPTION

J. Hueso-Rebassa[1], D. MacManus[1], F. Tejero[1], T. Williams[2], Y. Frey[3] & G. Thorne[3]

[1]Centre for Aeronautics, Propulsion and Power, Cranfield University
[2]Whittle Laboratory, Cambridge University
[3]Rolls-Royce plc

Abstract

This computational study investigates the coupled intake–fan aerodynamics and fan stability of a podded intake operating under crosswind conditions. Three crosswind velocities with different flow distortion characteristics were considered at constant fan speed while the fan was driven from the reference operating conditions to rotating stall. At low and medium crosswind velocities, the intake flow was attached from the lip at near-stall conditions. For these cases, the flow distortion was associated with the ground vortex, bulk swirl, local separations induced by the fan, and secondary flows induced by the ground vortex. Under these conditions, the fan stall margin was reduced by up to approximately 5% relative to an clean-flow single-passage baseline configuration. At the greatest crosswind velocity, the intake flow was grossly separated from the lip due to a shock induced separation. This resulted in a stall margin reduction of up to approximately 12%. Despite the different intake aerodynamic states at near fan stall conditions, there are some similarities in the onset of fan stall. Flow disturbances were generated at regions with increased blade incidence angle. These were related to reductions in axial velocity due to flow separation and tangential velocity increase due to the ground vortex. At fan stall conditions, the circumferential exposure to high incidence angles was sufficient to sustain the growth of disturbances into rotating stall cells. These results highlight the role of intake flow aerodynamics and unsteadiness in determining fan operability under crosswind conditions and underline the importance of coupled intake–fan assessments for aerodynamic design and stability analysis.

Keywords: Short intakes, crosswind, fan-intake coupling, fan stall inception, flow distortion

1. Introduction

1.1 Background

Future civil aero-engines are expected to adopt short intake designs [1] to support low specific thrust cycles and improve propulsive efficiency [2, 3]. However, short intakes introduce aerodynamic challenges under off-design crosswind conditions [4]. In crosswind, flow separation and vortex formation and ingestion may arise and induce unsteady total pressure and swirl distortion [1, 5]. Moreover, short intake configurations are likely to increase the aerodynamic coupling between the intake and the fan [6] which could be detrimental to the stability and performance of the turbomachinery components [7, 8].

1.2 Fan-intake coupling in crosswind

Intakes in crosswind are characterised by flow separation, a ground vortex and a trailing vortex depending on the operating conditions of crosswind velocity and Mass Flow Capture Ratio ($MFCR$) [9, 10]. At a fixed crosswind velocity and low $MFCR$, there is a subsonic, diffusion driven boundary layer separation at the windward aeroline [9, 10]. As $MFCR$ increases, the intake flow first reattaches and then separates through a shock-induced separation due to shock-boundary layer interactions

(SBLI) [9]. In addition, a pair of contra-rotating vortices may form due to the interaction of the intake capture stream tube and the ground (ground vortex and trailing vortex) [11, 12]. These aerodynamic features across the $MFCR$ range cause varying levels of total pressure and swirl distortion [9, 10] with an effect on the fan operability.

The intake aerodynamics can be notably influenced by the fan [6, 1, 14, 15, 16, 17]. The fan redistributes mass flow radially [6] and accelerates tip flow which may reduce adverse pressure gradients and delay separation [4]. However, unsteady effects, such as pressure waves from the fan, can reduce the crosswind velocity threshold for stable intake operation [6]. Boscagli et al. [6, 1] determined that the fan unsteadiness could reduce the crosswind velocity for flow separation by $4kts$ relative to a steady-state fan-intake system. This was due to the unsteady interactions between the upstream travelling fan waves, the ground vortex and the lip shock-wave. This triggered shock-induced separation through shock-boundary layer interactions (SBLI) at a lower crosswind velocity relative to steady computations. Lobuono et al. [13, 14] studied the unsteady interactions between an intake and a fan in crosswind for a range of intake lengths [14]. For short intake designs, shock-induced separation from the lip increased the blade incidence angle by up to 60^o relative to an undistorted baseline. Possible variations in blade incidence angle were considered through a method for the quantification of distortion in the relative frame of reference developed by Migliorini et al. [18]. This enabled the characterisation of distortion in metrics relevant to the fan performance and stability. Hueso-Rebassa et al. [10] applied the same relative frame of reference approach across a range of intake crosswind conditions and flow distortions. Diffusion and shock-induced separations were assessed with CFD for a model-scale intake coupled with a low-speed fan. Both types of flow separation increased the blade incidence by up to 60^o relative to a clean flow reference. The relative Mach number signature and unsteady characteristics of distortion were substantially different. Castillo Pardo et al. [15] investigated the effects of crosswind direction on the aerodynamics of a low-speed fan with CFD. In configurations with flow separation and a counter-rotating ground vortex, counter-swirl was induced at the blade tip which lead to higher work. Overall, it was found that the fan work was 6% higher for a counter-rotating ground vortex arrangement relative to a co-rotating configuration. These results demonstrated the importance of quantifying intake flow distortion with metrics that are relevant to the fan aerodynamics.

Although a significant amount of research has focused on short-intakes in crosswind and fan-intake coupling, these are all centred around the nominal operating conditions of the fan. Therefore, the effect of crosswind on the fan stability and fan stall inception remains unexplored.

1.3 Rotating stall inception in fans and compressors

Rotating stall occurs when stable flow can not be maintained over the compressor blades due to a low mass flow rate [20]. At a critical flow coefficient ($\phi = v_x/U$), disturbances are created at the blade tip, which can grow into rotating stall cells [20]. There are two distinguished routes to stall in compressors, modal stall and spike stall [21]. Modal stall occurs with the growth of long length scale oscillations in the operating point [20, 22], over tens of revolutions [23], while spike stall refers to the growth and propagation of small length scale disturbances [21, 20], typically developed over several blade pitches [21, 24]. Spike stall is the most common in aero-engines [20, 19].

Spike stall has been studied with clean [20, 19, 21] and distorted inlet flows [8, 20, 25, 26]. In general, the disturbance is caused by high incidence angles at the blade tip of the rotor leading edge [20]. This can trigger local flow separation at the suction side of the blade which forms a radial vortex that extends to the casing [21, 20, 23], increases local flow blockage on the blade passage and propagates to adjacent blades [21]. When these disturbances propagate they can decay or grow depending on the rotor operating conditions [20]. Spike-type stall has been identified in axial compressors with and without tip clearance [21]. The tip clearance defines the aerodynamic mechanisms leading to rotating stall. In shrouded rotors, the initial local flow separation is mainly related to corner flows between the casing and blade [24] while in configurations with tip clearance, the tip leakage flows also play a role [23].

Inlet flow distortion always reduces stability relative to clean inflow conditions [20, 8]. Canonical distortion configurations such as ingested vortices [8] and circumferential [20, 25] and radial [26] total pressure distortion have been assessed. Awes et al. [8] investigated the effects of vortex ingestion

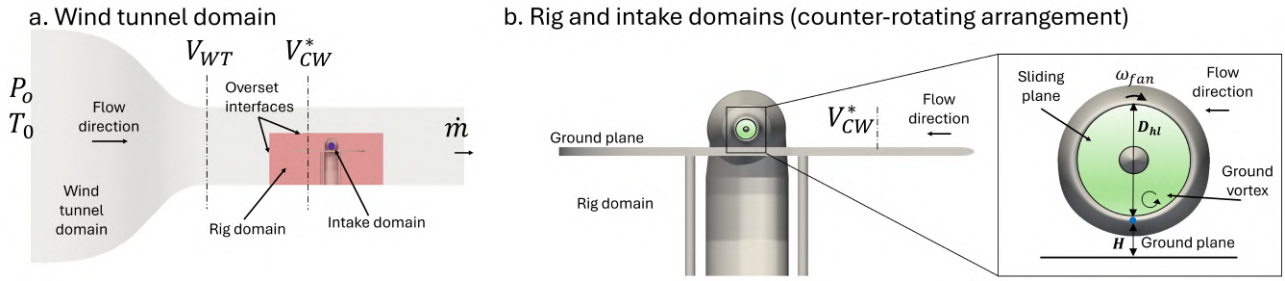


Figure 1 – (a) Schematic of the wind-tunnel and (b) intake rig arrangements. This is for a crosswind counter-rotating (port) configuration. Figure adapted from [10].

on the operability of Ultra-High Bypass Ratio (UHBR) fans. It was concluded that the stall inception mechanism was similar for clean flow and vortex ingested configuration. However, the vortex ingestion resulted into a stall margin loss of up to 8%. Allen et al. [25] studied the circumferential extend of tip total pressure distortion in fan stability experimentally. Although the effects of flow distortion did not change the fan stall mechanism relative to clean inflow conditions, it impacted the stall margin. For full circumferential tip distortion the stall margin was reduced by 8% while for a half annulus configuration it was reduced by 4%. Williams et al. [26] investigated the effects of radial distortion into the stall inception of low pressure ratio transonic fans. This was with experiments and CFD that included a perforated plate to generate distortion. According to the experimental results, the inlet distortion reduced the stall margin by $\approx 8\%$ relative to the clean flow conditions. The case with distortion presented a lower stall flow coefficient at the tip, which moved the leading edge shock upstream and increased blockage.

Although there has been substantial research in the effects of flow distortion into fan stall inception [8, 20, 25, 26], most of the work focuses in canonical flow distortion patterns that assess swirl and total pressure distortion independently, in laboratory environments. Short intakes in crosswind may induce multiple sources of flow distortion simultaneously. These may encompass several classes of flow separation [9, 10] and vortices [11, 12] which combine swirl and total pressure distortion. These directly impact the blade incidence angle and may result into longer circumferential extents where the blade is exposed to critical conditions. Therefore it is of interest to investigate the intake crosswind aerodynamics and the impact it has into the fan stability and inception of rotating stall.

1.4 Overview and Scope

This work investigates the coupled intake–fan aerodynamics of a short, podded intake operating under crosswind conditions with unsteady CFD. Three crosswind velocities with a counter-rotating ground vortex and varying levels of flow distortion are considered at constant fan speed. The fan is driven to stall under these conditions to assess the impact of the intake aerodynamics and flow distortion on fan performance, stability margin and onset of rotating stall. The novelty of this study is the assessment of the effect of intake crosswind velocity onto the fan stall inception. The contribution is new quantitative evidence that indicates how attached and grossly separated intake flows influence fan stall margin. In addition, it demonstrates that while there are similarities in the fan stall inception mechanism across crosswind conditions, the overall intake flow state governs the operating point at which stall occurs. These findings improve the understanding of intake–fan compatibility under crosswind operation.

2. Methodology

2.1 Short intake coupled with a fan in crosswind

This work is focused on a model-scale short intake coupled with a low-speed fan and installed in a wind tunnel [27, 10]. The intake is non-axisymmetric with a normalised intake length (L_{int}) over fan diameter (D_{fan}) of $L_{int}/D_{fan} = 0.33$ [27, 10]. In the crosswind configuration, the intake-fan system is coupled with a ground plane with a clearance of $H/D_{hi} = 0.3$ (Fig. 1, [10]). The baseline datum

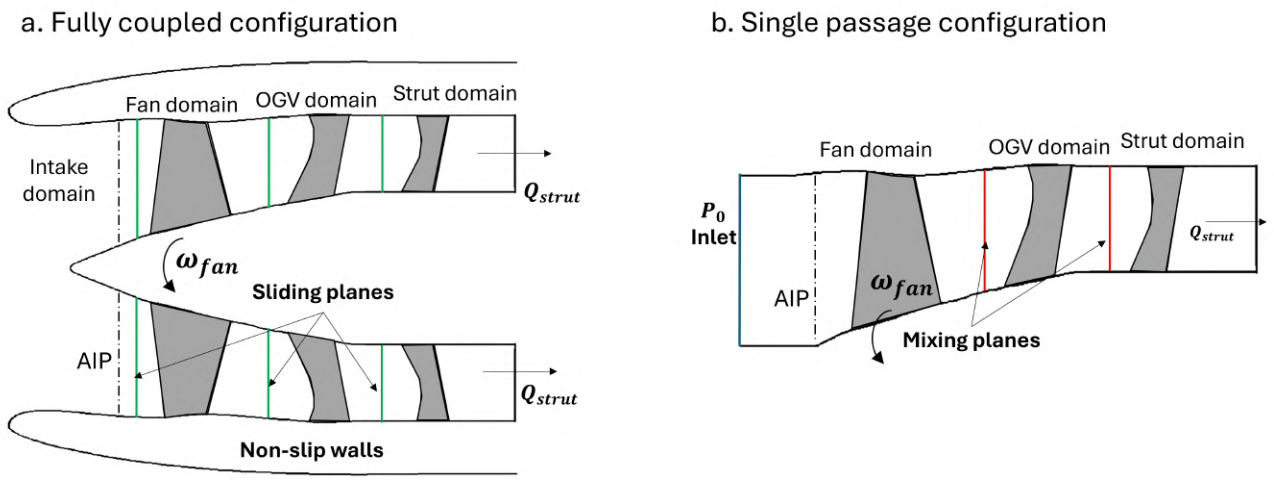


Figure 2 – Schematic of computational configurations. (a) Fully coupled intake-fan-OGV-strut system and (b) single passage configuration. Figure adapted from [10].

arrangement is a port configuration where the air flows from the right, looking at the intake from upstream. This configuration induces a ground vortex that is counter-rotating with the fan (counter-rotating configuration, Fig. 1).

2.2 Computational modelling

The fan-intake rig configuration was assessed with unsteady CFD at a range of crosswind conditions. The unsteady, compressible Favre-averaged Navier-Stokes equations were solved with a double precision, implicit density-based solver [28]. The CFD solver was combined with the $k-\omega$ SST turbulence model [29], a second-order MUSCL convective scheme [30] and the Green-Gauss node based method [31] to approximate the flow gradients. Dynamic viscosity as a function of temperature was modelled with Sutherland's law [32]. The temporal resolution of the simulations was 90-time steps per blade passing time (t_{bp}) with an implicit temporal scheme [10]. The simulations run for 8 full fan revolutions after numerical transient decayed. These were found sufficient to achieve periodicity and develop rotating stall.

The unsteady (URANS) simulations used six independent computational domains. These encompassed a wind tunnel, rig mount with a ground plane, short intake, full-annulus rotating fan, full-annulus outlet guide vanes (OGVs), and struts after the OGVs (Fig. 2a) [10]. The intake and rig domains were overset onto the wind tunnel domain through an overlapping interface at the boundaries of the sub-domains [33, 34], while the fan, OGVs, and struts were coupled through sliding planes at the interfaces (intake-fan, fan-ogv and ogv-struts). Total pressure (P_0) and total temperature (T_0) were prescribed at the wind tunnel and static pressure (P) with a target mass flow at the exit (Fig. 1a). The wind tunnel conditions were calibrated to achieve target flow velocities at the entry of the rig test section (V_{WT}, Fig. 1). All the walls of the wind tunnel, rig, intake and turbomachinery components were viscous non-slip. The intake ingested mass flow was set through a capacity ($Q_{strut} = \dot{m}\sqrt{(T_0)}/(P_0 A)$ boundary condition prescribed at the strut outlet plane (Fig. 2). Unsteady simulations started at the reference operating conditions of the fan. To evaluate the onset of stall, Q_{strut} was reduced while maintaining the fan rotational speed ($N/\sqrt{(T_0)}$) until stall cells formed at the fan.

In addition to the unsteady CFD simulations, steady RANS computations of single passage sectors of the fan, OGV and struts were also carried out (Fig. 2b). These were periodic and the turbomachinery components were coupled through mixing planes. The objective of these simulations was to determine an idealised flowfield with no intake distortion (Fig. 2b). The single passage calculations were at the same speed-line as the unsteady crosswind CFD and also run until fan stall.

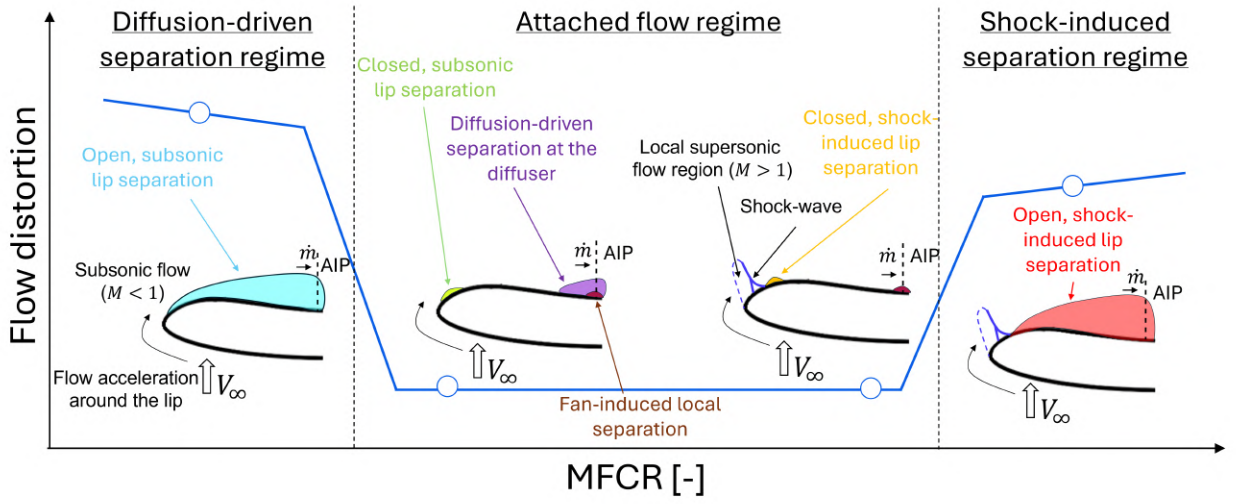


Figure 3 – Schematic of the different intake aerodynamic regimes in crosswind. This is for a fixed crosswind velocity with varying $MFCR$.

2.2.1 Computational grids

Independent grids were created for the wind tunnel, rig, intake, fan, OGV and struts. The intake and turbomachinery meshes were generated with a multi-block structured approach with a $y^+ = 1$. The grids for the wind tunnel and rig were developed in STAR-CCM+ with a hybrid approach [35] that combined unstructured tetrahedral cells and structured prism layer near the viscous walls, with a $y^+ \approx 50$ [35]. The solver used wall functions when needed based on an automatic activation which was triggered when y^+ was below 5 [28].

The spatial discretisation of the wind tunnel, rig and intake meshes was based on a grid sensitivity study without the turbomachinery components (aspirated intake configuration). The details of the process are reported in Hueso-Rebassa et al. [10]. It was found that both medium and fine meshes captured the reduction of total pressure distortion descriptor (DC_{60}, [36, 37]) related to flow reattachment across a range of intake mass flows at a fixed wind tunnel velocity V_{WT}. Therefore, the medium meshes with a total of 114.2×10^6 cells were selected. For the turbomachinery domains, the grids were based on previous guidelines [38]. The fan rotor, OGVs and struts had 75.0×10^6, 78.0×10^6 and 8.0×10^6 cells, respectively. Overall, the complete computational configuration had approximately 298×10^6 cells.

2.3 Intake performance in crosswind

The intake performance in crosswind is characterised by the Mass Flow Capture Ratio ($MFCR$, Eq. 1) and crosswind velocity. The $MFCR$ is defined with the intake mass flow ($\dot{m}$), the intake highlight area (A_{hi}), the effective crosswind velocity (V^*_{CW}) and the free-stream density (ρ_∞). The intake mass flow is function of the fan operating conditions of Q_{fan} (Eq. 9) which is controlled through the capacity at the exit of the strut stage (Q_{strut}), imposed as the CFD boundary condition. The effective crosswind velocity is measured $5D_{hi}$ upstream of the intake center line (Fig. 1) and accounts for the wind tunnel aerodynamic blockage. V^*_{CW} is a linear function of the wind tunnel velocity V_{WT} at the entry of the test section [10].

$$MFCR = \frac{\dot{m}}{\rho_\infty V^*_{CW} A_{hi}} \tag{1}$$

The combination of $MFCR$ and crosswind velocity defines the broad aerodynamic state of the intake flow [9, 10]. A ground vortex may appear at moderate values of $MFCR$ [11]. At fixed crosswind velocity and low $MFCR$ (Fig. 3), the intake flow can be separated from the lip through a subsonic diffusion led separation. With increasing $MFCR$, the flow first reattaches at the lip and then separates again through a high-speed shock-induced mechanism [9, 10]. In addition to the gross separation

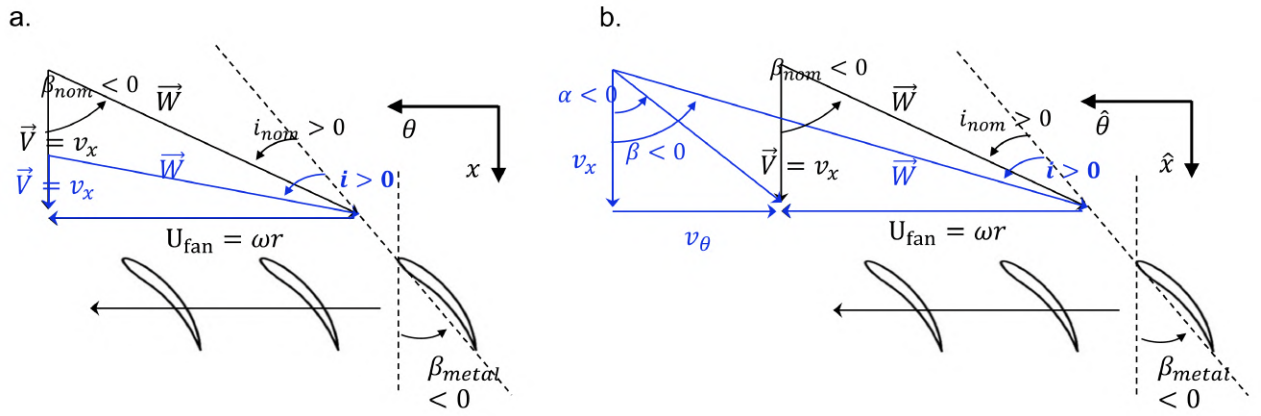


Figure 4 – Examples of velocity triangles where black represents the ideal axial flow and blue are examples with flow distortion. (a) Distorted flow with a reduction in axial velocity and (b) distorted flow with counter-rotating swirl.

from the lip, other local closed separation regions may appear within the attached flow regime (Fig. 3). These can be subsonic, shock-induced, diffusion driven and due to the upstream effects of fan (Fig. 3) [10]. Multiple separation mechanisms may be present at the same time and become undistinguishable. A more thorough evaluation of the intake flow separation mechanisms in crosswind can be found in the literature [10]. Throughout this work, the intake separation is identified as whether there is reversed mass flow (m^-) through the Aerodynamic Interference Plane (AIP) such as $m^- > 0.001\%$ [6, 10].

2.4 Methods for the analysis of intake distortion

Unsteady results were analysed in terms of total pressure recovery ($PR = P_0/P_{0,\infty}$) and swirl angle (α) distributions at the Aerodynamic Interference Plane (AIP), isentropic Mach number (M_{is}) and stream-wise wall shear stress (τ_x) distributions at the intake surface to determine the overall aerodynamic characteristics. The AIP was positioned $0.05D_{fan}$ upstream of the blade hub leading edge. The flow distortion was analysed in the relative frame of reference to study the influence of the intake flow on the fan stall inception. The relative frame of reference approach takes temporal and spatial variations of the unsteady intake distortion into account. This is to quantify the changes in blade incidence angle (i) and relative Mach number (M_{rel}) as the intake-fan system approaches the fan stall point. The methodology is detailed in previous works [18, 14, 10].

The flow velocity in the absolute reference frame is $\vec{V} = \{v_x, v_r, v_\theta\}$ in cylindrical coordinates, with axial ($\hat{x}$), radial ($\hat{r}$) and tangential ($\hat{\theta}$) components. The tangential coordinate is defined positive in the clock-wise direction. The relative velocity vector ($\vec{W}$, Eq. 2) is the vectorial difference between the absolute flow velocity ($\vec{V}$) and the local tangential speed of the fan ($U_{fan} = r\omega_{fan}$). The relative Mach number (M_{rel}, Eq. 3) is calculated with $\vec{W}$ the local speed of sound (a).

$$\vec{W} = \{w_x, w_r, w_\theta\} = \{v_x, v_r, v_\theta - \omega_{fan} r\} \tag{2}$$

$$M_{rel} = \frac{\|\vec{W}\|}{a} = \frac{\sqrt{v_x^2 + v_r^2 + (v_\theta - \omega_{fan} r)^2}}{a} \tag{3}$$

The absolute swirl angle (α, Eq. 4, Fig. 4) is the angle between the absolute tangential velocity (v_θ) and the axial velocity (v_x) and is defined positive in the clockwise direction. The relative flow angle (β, Eq. 5, Fig. 4) is the angle between the axial velocity component and the relative tangential velocity component (w_θ) and is also positive in the clockwise direction. The relative blade incidence angle (i) at the fan leading edge is defined as the difference between the local flow angle (β) and the blade metal angle at the leading edge (β_{metal}, Eq. 6) and is positive in the counter-clockwise direction. The definition of the different angles and polarity is illustrated in the velocity triangles (Fig. 4).

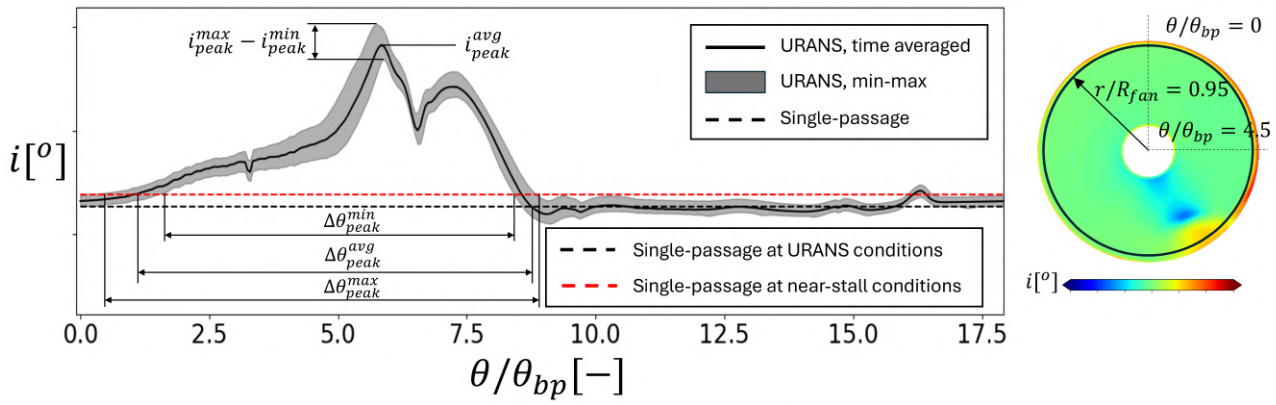


Figure 5 – Example of blade incidence angle (i) variation at $r/R_{fan} = 0.95$. The figure includes URANS crosswind results, single passage results and the definition of peak incidence values (i_{peak}) and azimuthal extends of distortion ($\Delta\theta_{peak}$). The red, dashed line indicates the near-stall conditions of the single-passage configuration ($i_{sp}^{near-stall}$).

$$\alpha = \arctan\left(\frac{v_\theta}{v_x}\right) \tag{4}$$

$$\beta = \arctan\left(\frac{w_\theta}{v_x}\right) \tag{5}$$

$$i = \beta_{metal} - \beta \tag{6}$$

The blade incidence angle and relative Mach number were evaluated on a ring located at 95% of blade radius ($r/R_{fan} = 0.95$), on the AIP. This enabled the calculation of variations of i, M_{rel} and v_x relative to the single-passage, baseline configuration where there is no intake or intake flow distortion (Fig. 5). For unsteady simulations of intakes in crosswind, it is of interest to calculate the blade incidence angle relative to a baseline conditions (Δi, Eq. 7). In this approach, Δi is calculated relative to the blade incidence angle of the single passage configuration at near stall conditions ($i_{sp}^{near-stall}$, Fig. 5, in red) . Therefore, $i_{sp}^{near-stall}$ is a blade incidence threshold which enables the calculation of the azimuthal extent of peak distortion relevant to the fan stall inception ($\Delta\theta_{peak}$, Fig. 5) [20]. In addition to the extents, peak values of blade incidence angles are also computed (i_{peak}) as these are likely to impact the fan stall margin (Fig. 5). For both metrics ($\Delta\theta_{peak}$ and i_{peak}), time averaged ($\Delta\theta_{avg}^{avg}$ and i_{peak}^{max}), minimum ($\Delta\theta_{peak}^{min}$ and i_{peak}^{min}) and maximum ($\Delta\theta_{peak}^{max}$ and i_{peak}^{max}) values are considered to quantify the unsteadiness due to intake flow distortion (Fig. 5).

$$\Delta i = i - i_{sp}^{near-stall} \tag{7}$$

The flow coefficient (ϕ, Eq. 8) Another metric of interest for the quantification of the effects of intake crosswind aerodynamics into fan operability. It is defined as the axial velocity (v_x) normalised by the local blade speed ($U_{fan} = \omega r$). Similar to the blade incidence angle and relative Mach, local ϕ is also evaluated over a ring located at $r/R_{fan} = 0.95$ and expressed relative to the flow coefficient of the single passage configuration at near stall conditions ($\Delta\phi = \phi - \phi_{sp}^{near-stall}$)

$$\phi = \frac{v_x}{U_{fan}} \tag{8}$$

2.5 Fan stability margin and stall identification

The fan metrics of interest are the capacity (Q_{fan}, Eq. 9) at the fan inlet and total pressure ratio (π, Eq. 11), isentropic efficiency (η, Eq. 12) and stall margin (κ, Eq. 13 [26]). The fan capacity

(Eq. 9) is calculated with the mass flow through the turbomachinery components corrected for ambient conditions ($\dot{m}_{cor}$, Eq. 10) and the Mass Mean Mixed Out (MMMO) average total pressure, total temperature and area (A_{AIP}) at the Aerodynamic Interference Plane (AIP).

$$Q_{fan} = \frac{\dot{m}_{cor}\sqrt{T_0^{AIP}}}{P_0^{AIP} A_{AIP}} \tag{9}$$

$$\dot{m}_{cor} = \dot{m}\sqrt{\frac{T_0}{T_0^{sl}}}\frac{P_0^{sl}}{P_0} \tag{10}$$

The total pressure ratio (π, Eq. 11) is calculated with the MMMO averages of total pressure at the AIP (P_0^{AIP}) and total pressure at the outlet of the fan domain (P_0^{outlet}) while the definition of isentropic efficiency (η, Eq. 12) also includes MMMO averaged values of total temperature at the same stations and the ratio of specific heats (γ).

$$\pi = \frac{P_0^{outlet}}{P_0^{AIP}} \tag{11}$$

$$\eta = \frac{\left(\frac{P_0^{outlet}}{P_0^{AIP}}\right)^{\frac{\gamma-1}{\gamma}} - 1}{\frac{T_0^{outlet}}{T_0^{AIP}} - 1} \tag{12}$$

The stall margin (κ, Eq. 13) is derived from changes in 1D throttle area (A_e) [26]. It is calculated with the corrected mass flow and total pressure ratio between the reference (super index ^{ref}) and near-stall fan operating conditions (super-index *). The near-stall conditions are the last stable operation of the fan. Within this work, the fan stall margin is expressed as a reduction of κ ($\Delta\kappa$, Eq. 14) relative to the single passage idealised calculations (κ_{id}). This is to assess the effect of intake flow distortion on the fan stability. To identify the development of spike stall cells, static pressures traces are extracted at twelve probes along the fan casing, near the fan leading edge at the tip. A low-pass filter is applied to remove the frequency content associated with the blade passing frequency (f_{bp}) [26, 21]. Therefore, there are are three operating conditions of interest: the reference operating conditions, the near stall conditions and ultimately the fan stall point.

$$\kappa = \frac{A_e^{ref} - A_e^*}{A_e^{ref}} = 1 - \frac{\dot{m}_{cor}^*}{\dot{m}_{cor}^{ref}}\frac{\sqrt{(\pi^{ref})^{(\gamma-1)/\gamma} - 1}}{\sqrt{(\pi^*)^{(\gamma-1)/\gamma} - 1}} \tag{13}$$

$$\Delta\kappa = \kappa_{id} - \kappa \tag{14}$$

3. Results and discussion

3.1 Intake crosswind aerodynamics to fan stall

Three crosswind velocities ($V_{CW} = V_{CW}^{ref} - 5kts$, V_{CW}^{ref} and $V_{CW}^{ref} + 10kts$) were investigated for a counter-rotating configuration at a fixed fan speed ($N/\sqrt{T}$). The three crosswind conditions are at a different locations in the crosswind performance map defined by the Mass Flow Capture Ratio ($MFCR$) and crosswind velocity (Fig. 6) and therefore have notable differences in terms of the intake aerodynamics through the development of fan stall (Fig. 6 and 7). At $V_{CW} = V_{CW}^{ref} - 5kts$, and reference operating conditions of the fan, the intake flow is predominately attached and remains attached until the fan stall point (Fig. 6 and 7a). At V_{CW}^{ref} and reference Q_{fan}, the intake flow is grossly separated from the lip through a shock-induced separation (Fig. 6 and 7b). However, when the fan capacity is reduced in the progress towards the fan stall point, the intake lip shock weakens and the flow reattaches (Fig. 6 and 7b). Therefore, at the near fan stall conditions the intake flow is attached from the lip, similar to the $V_{CW} = V_{CW}^{ref} - 5kts$ case. At a greater crosswind velocity ($V_{CW}^{ref} + 10kts$), the intake flow is grossly separated from the lip through a shock-induced separation at the reference fan operating conditions and all the way to the stall point (Fig. 6 and 7c). In addition to the lip gross separation,

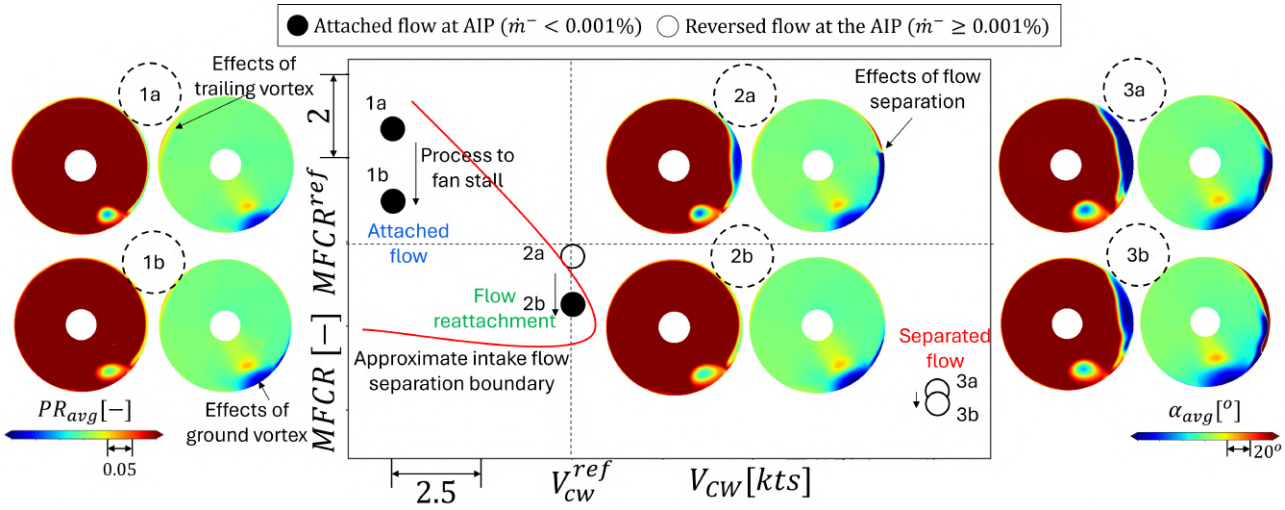


Figure 6 – Intake crosswind performance map and time-averaged distributions of Pressure Recovery (PR_{avg}) and swirl angle (α_{avg}) at the AIP. The figure includes the distributions at the reference fan operating conditions and near stall for $V_{CW} = V_{CW}^{ref} - 5kts$, $V_{CW} = V_{CW}^{ref}$ and $V_{CW} = V_{CW}^{ref} + 10kts$.

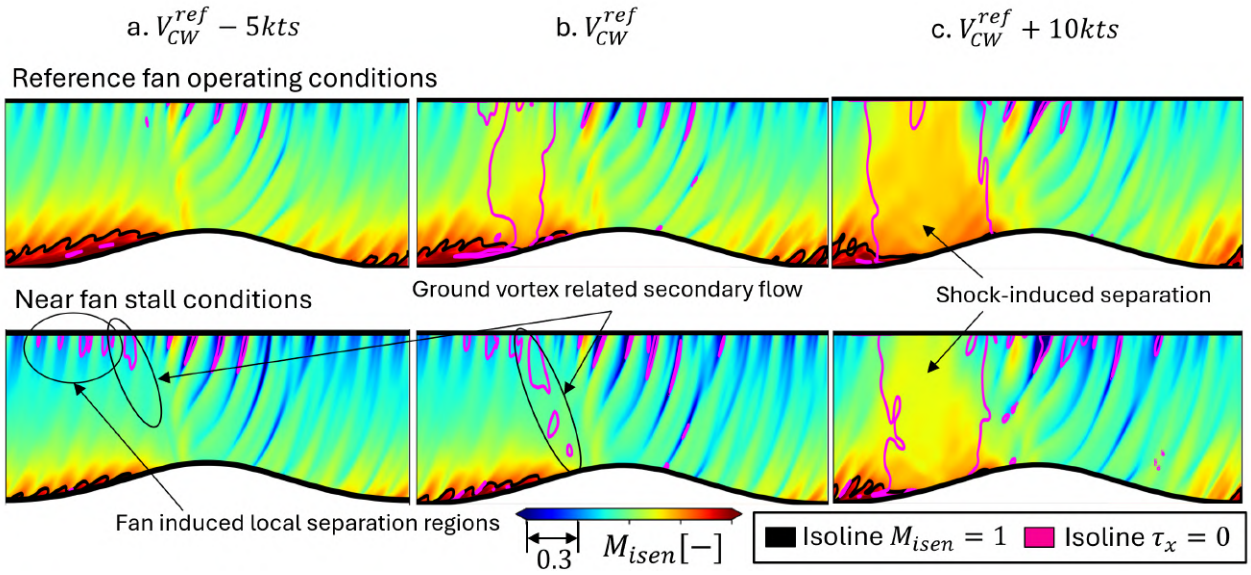


Figure 7 – Snapshots of isentropic Mach number (M_{is}) over the unwrapped intake surface. The figure includes the distributions at the reference fan operating conditions and near rotating stall for $V_{CW} = V_{CW}^{ref} - 5kts$, $V_{CW} = V_{CW}^{ref}$ and $V_{CW} = V_{CW}^{ref} + 10kts$.

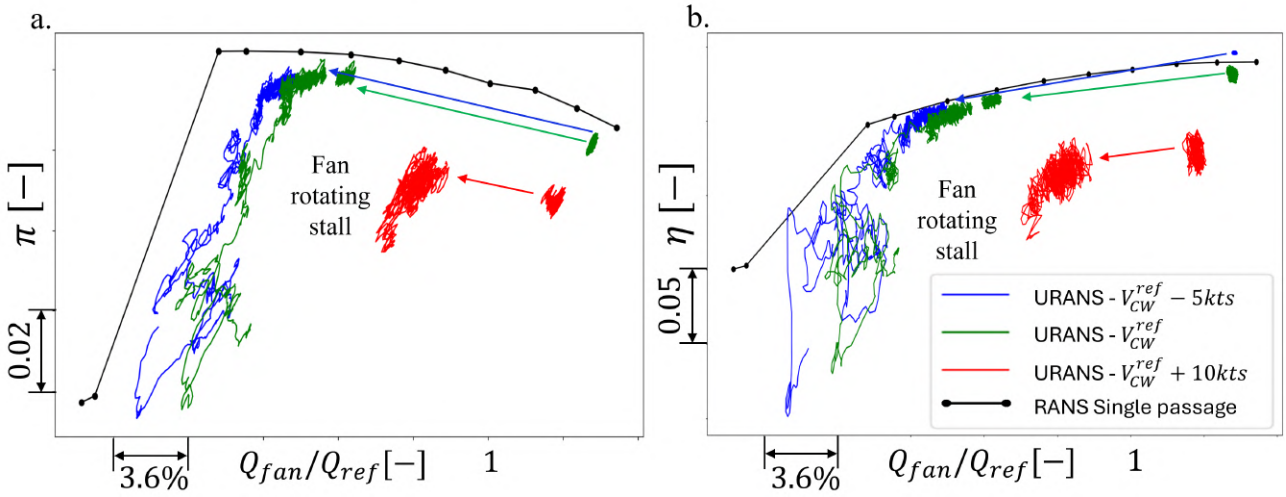


Figure 8 – Fan performance maps for different crosswind velocities. (a) Fan rotor total pressure ratio (π) and (b) isentropic efficiency (η).

the three crosswind conditions also have local flow separation regions. These include supersonic separation with reattachment at the lip, fan-induced unsteady separation regions within the intake diffuser and local flow unsteady separations related to the ground vortex secondary flows. These effects are more notable at the near-stall conditions for the cases with $V_{CW} = V_{CW}^{ref} - 5kts$ (Fig. 7a) and V_{CW}^{ref} (Fig. 7b). Within this work, this type of flow distortion associated with the feature is found to have an important role in the development of fan stall cells (Fig. 7).

The intake aerodynamics can change substantially in the progress to fan stall conditions. As Q_{fan} is reduced (and consequently $MFCR$) the intake flow could reattach, or potentially separate through diffusion separation (Fig. 3) which can impact the fan stall margin. Therefore, the intake aerodynamics at the reference fan operation is not representative for the quantification of stability margin.

3.2 Effect of intake crosswind aerodynamics on fan performance and stability

The effect of crosswind velocity and intake flow distortion on the fan performance and stability was assessed on the fan rotor capacity (Q_{fan}) the total rotor pressure ratio (π, Fig 8a), isentropic efficiency (η, Fig. 8b) and stall margin (κ, Table 1). At the lowest crosswind velocity ($V_{CW} = V_{CW}^{ref} - 5kts$) and at the reference operating conditions of the fan, π and η remain similar relative to the single passage configuration (Fig. 8). However, there is a reduction of 1% in Q_{fan} due to the increased loses in P_0. At the same conditions, the stall margin loss is $\Delta\kappa = 3.7\%$ relative to the fan stall conditions of the single passage configuration (Fig. 8, Table 1). These effects are primarily driven by the ground vortex, bulk swirl and local regions of flow separation at the intake diffuser (Fig. 6 and 7). The increased crosswind speed ($V_{CW} = V_{CW}^{ref}$) reduces π, η and fan stall margin slightly ($\Delta\kappa = -5.0\%$) relative to the $V_{CW} = V_{CW}^{ref} - 5kts$ case. This was due to the effects of the ground vortex strength and bulk swirl at 5kts greater crosswind velocity.

V_{CW} [kts]	Intake flow separation	Stall margin loss [%]
$V_{CW}^{ref} - 5$	No	-3.7
V_{CW}^{ref}	Only at reference conditions	-5.0
$V_{CW}^{ref} + 10$	Yes	-11.6

Table 1 – Summary of intake aerodynamics and fan stall margin loss relative to the baseline single passage calculations.

The reduction of Q_{fan}, π, η and stability margin is more notable at $V_{CW} = V_{CW}^{ref} + 10kts$ (Fig. 8).

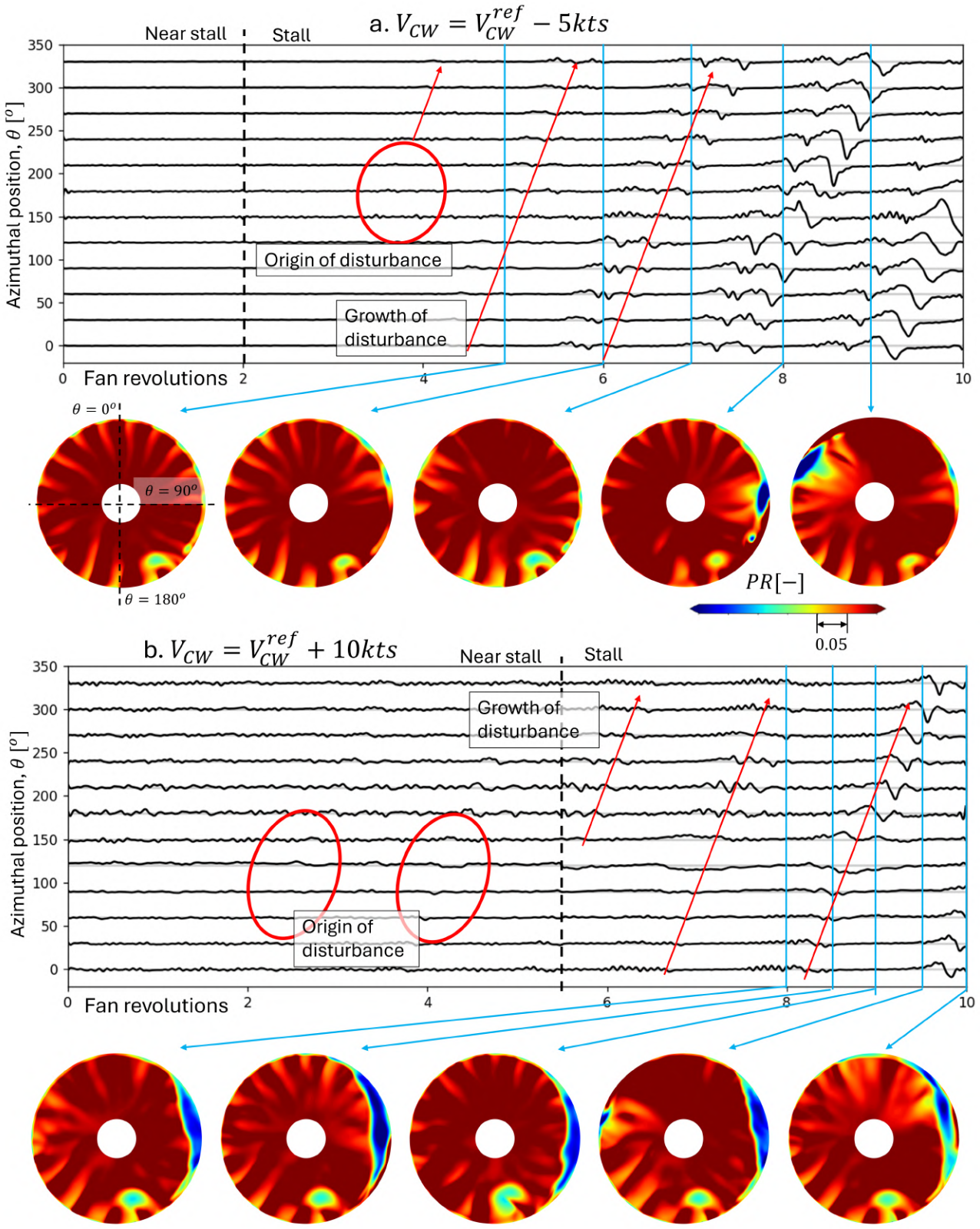


Figure 9 – Azimuthal signatures of static pressure at the fan casing and distributions of PR at the AIP (snapshots) for several time steps along the fan stall formation. (a) $V_{CW} = V_{CW}^{ref} - 5kts$ and (b) $V_{CW} = V_{CW}^{ref} + 10kts$. The figure includes filtered time signals with $f_{cut} = \frac{1}{2} f_{bp}$.

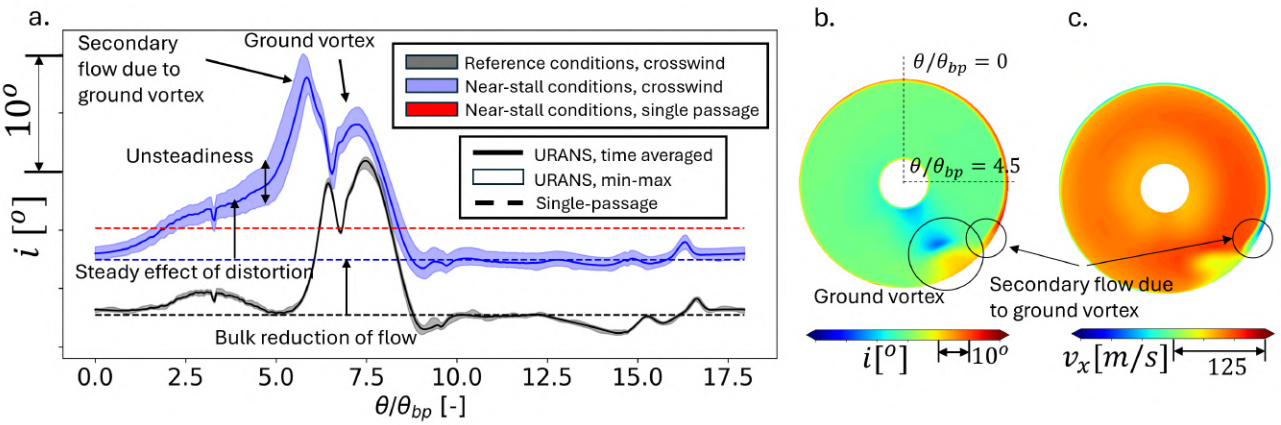


Figure 10 – (a) Variation of blade incidence angle (i) at $r/R_{fan} = 0.95$, (b) time averaged i and (c) v_x distributions at the AIP, for the case at $V_{CW} = V_{CW}^{ref} - 5kts$.

The effects of the shock-induced separation from the lip (Fig. 6 and 7c) reduce Q_{fan} the total rotor pressure ratio and efficiency by 3.5%, 0.02 and 7.5%, respectively, relative to the single passage configuration with clean flow (Fig. 8). This is mainly due to the P_0 losses at the intake due to the shock-induced separation. The loss of stall margin is of $\Delta\kappa = -11.6\%$ relative to the single passage clean-flow configuration (Table 1). Fan stall was identified through the static pressure traces at the fan casing, near the blade tip leading edge (Fig. 9). The traces indicate the classic signature of spike-type rotating stall, where the disturbance grows across several blade pitches [21, 24]. The traces are examined in more detail in section 3.4.

In conclusion, for an attached intake flow where the distortion is mostly related to swirl the stall margin is reduced by up to 5% relative to the baseline clean-flow configuration. This is lower relative to the literature where a prescribed, single ingested vortex reduced the stall margin by up to 8% [8]. The difference could be partially attributed to the presence of a co-rotating trailing vortex in crosswind (Fig. 6) which induces co-swirl at the leeward aeroline and reduces blade incidence angle at the blade tip. This effect can reduce the extent in which the blade is subject to higher incidence angles with a delay in the stall cell growth [20]. However, when the intake flow is grossly separated, the impact on the fan stability is more notable and can erode the fan stall margin by up to $\Delta\kappa = -11.6\%$. The loss in stall margin is greater relative to canonical cases where circumferential [25] and radial [26] total pressure distortion at the blade tip reduced stall margin by up to 8%. For separated intakes in crosswind, the flow separation and the ground vortex may lead to an increased azimuthal extent of high incidence angles and diminish the stall margin. These results highlight the impact of crosswind velocity on the stall margin of the fan and the need to include realistic intake flow aerodynamic states for the assessment of fan operability.

3.3 Effect of crosswind velocity at near-stall conditions

To investigate how the intake flow distortion influences the onset of fan stall, an analysis of the aerodynamics in the relative frame of reference was considered at the near stall conditions. The blade incidence angle (i), M_{rel} and flow coefficient (ϕ) distributions were assessed at $r/Rfan = 0.95$ for the three crosswind velocities (Fig. 10 and 11). This was based on the full set of unsteady data and considered both the spatial and temporal variations. In figures 10 and 11, black indicates the reference Q_{fan} conditions (crosswind), blue represents the values at near-stall (crosswind) and red is the near-stall solution of the single passage baseline CFD, which is used as a threshold [20].

For the case at $V_{CW} = V_{CW}^{ref} - 5kts$ and at the reference Q_{fan} (Fig. 10 and 11a, black), the maximum blade incidence angle is about 15^o above the single passage configuration at the same conditions. The increase in i is due to the counter-rotating ground vortex ($\theta/\theta_{bp} = 7.5$) as the intake flow is predominantly attached. The ground vortex also increases M_{rel} (Fig. 11a). In addition, there is a second region of increased incidence at $\theta/\theta_{bp} = 3$ (Fig. 10). This is dominated by the reduction in

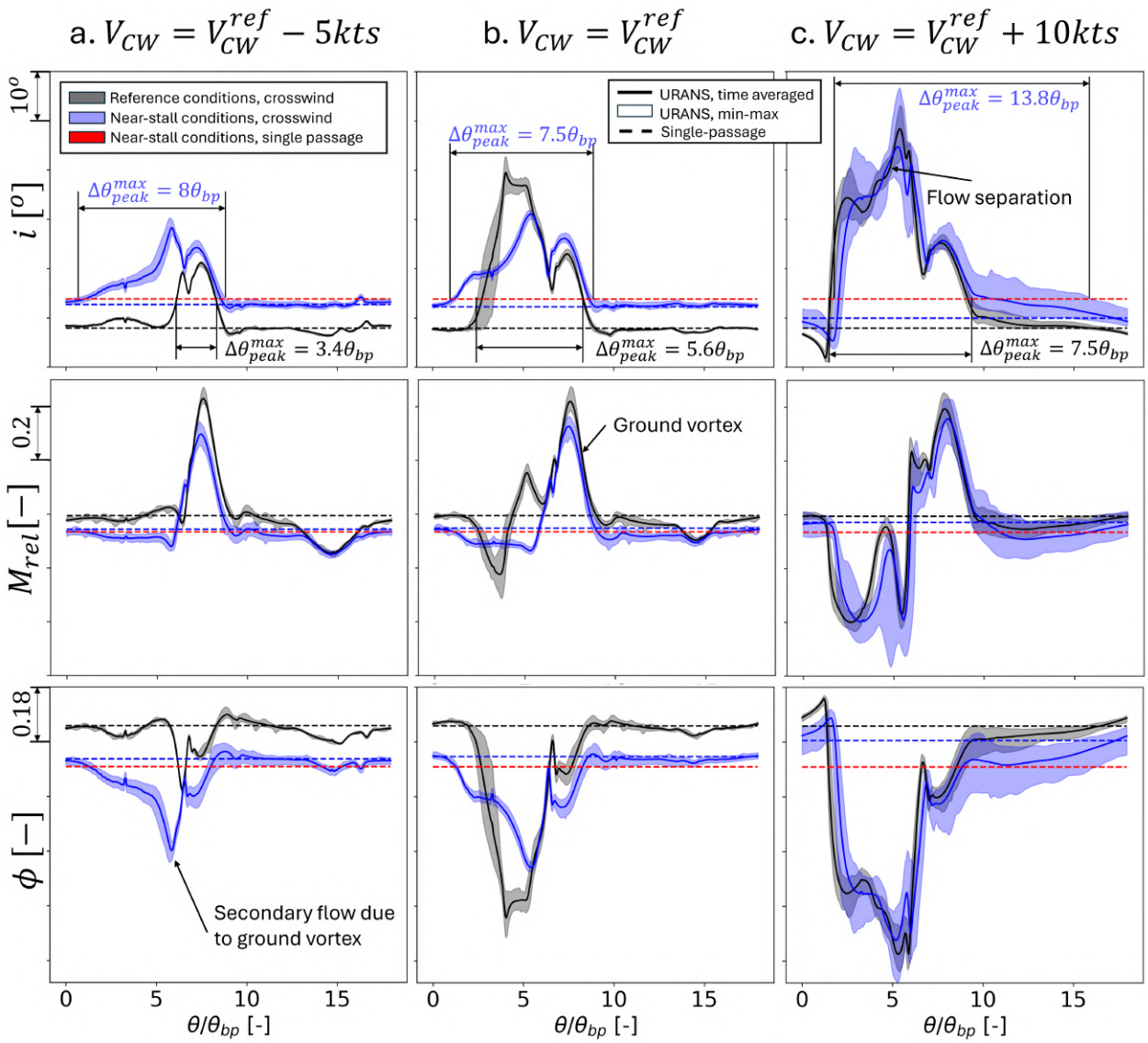


Figure 11 – Blade incidence angle (i), relative Mach (M_{rel}) and flow coefficient (ϕ) distributions at $r/R_{fan} = 0.95$ and at the AIP. (a) $V_{CW} = V_{CW}^{ref} - 5kts$, (b) $V_{CW} = V_{CW}^{ref}$ and (c) $V_{CW} = V_{CW}^{ref} + 10kts$.

flow coefficient at the diffuser part of the intake, at the windward side, and it also reduces M_{rel} (Fig. 11a). This effect is related to the fan-induced separation pockets at the windward side and secondary flows related to the ground votex (Fig. 7a). However, these two regions of incidence distortion are independent and therefore the fan can potentially recover between these events. As the system approaches the fan stall point, the two regions of increased incidence merge and the impact on the fan persists for a longer azimuthal extend (Fig. 10 and 11a, blue). At near-stall conditions, the peak incidence angle is encountered before the ground vortex, at the region with reduced M_{rel} and ϕ (Fig. 11a, blue). The peak value of incidence is related to the secondary flow induced by the ground vortex which produces a local region of separation (Fig. 7a). This induces unsteadiness in axial velocity (flow coefficient) which results in a variation of blade incidence of $\pm 2.5^o$ (Fig. 10, blue).

For the case at the reference crosswind velocity ($V_{CW} = V_{CW}^{ref}$), the intake is separated at the reference fan operating conditions. However, as the flow reattaches in the progress to the fan stall conditions, the intake aerodynamics in terms of blade incidence angle, M_{rel} and v_x (Fig. 11b) is very similar to the case at $V_{CW} = V_{CW}^{ref} - 5kts$, with peak incidence angle also caused by the secondary flows related to the ground vortex (Fig. 7b and 11b). At the highest crosswind velocity ($V_{CW} = V_{CW}^{ref} + 10kts$), the intake flow is grossly separated from the reference Q_{fan} conditions to the fan stall point. At the reference Q_{fan} the maximum blade incidence angle is about 50^o above the single passage baseline.

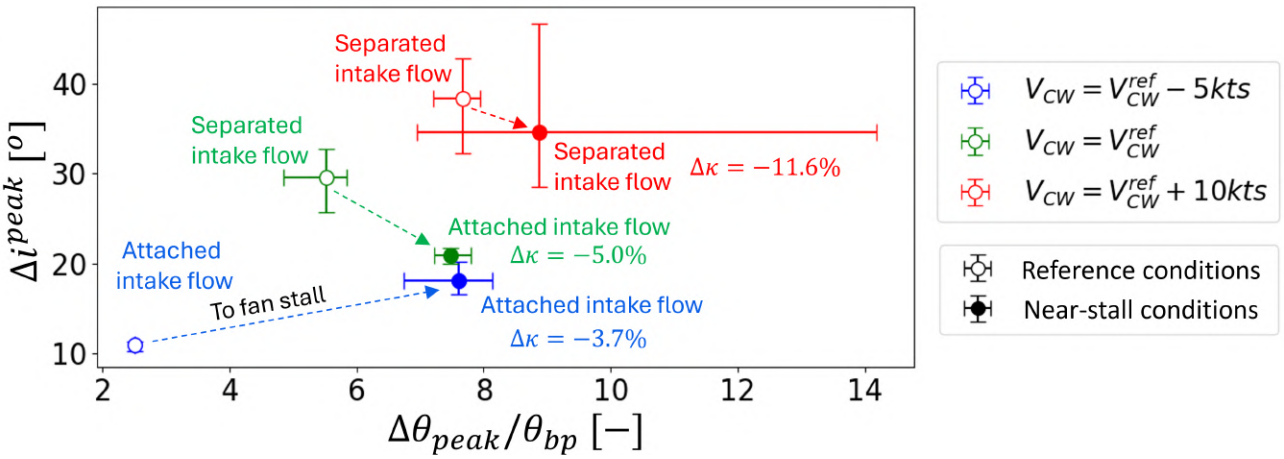


Figure 12 – Effect of crosswind velocity on the peak blade incidence angle (Δi^{peak}) and peak exposure to distortion ($\Delta\theta_{peak}$). The figure includes the reference Q_{fan} and near-stall conditions for the three crosswind velocities.

However, at these conditions the peak values are related to the gross shock-induced flow separation ($\theta/\theta_{bp} = 2.25$ to 6.75). The peak incidence angles and lowest values of relative Mach are again encountered right before the ground vortex ($\theta/\theta_{bp} = 6.75$). This is an indication of the effects of the secondary flow related to the ground vortex, which is similar to the cases with attached intake flow ($V_{CW} = V_{CW}^{ref} - 5kts$ and $V_{CW} = V_{CW}^{ref}$). Similar to the configurations at lower crosswind velocity ($V_{CW} = V_{CW}^{ref} - 5kts$), the unsteadiness in blade incidence angle, ϕ and relative Mach increases approaching the fan stall conditions (Fig. 11c,blue). Although the peak incidence angle is similar at the reference operating conditions and near-stall, the flow unsteadiness after the ground vortex leads to substantially longer exposures to distortion in terms of blade incidence angle and flow coefficient.

Peak incidence angles (Δi^{peak}) and peak exposures to incidence distortion ($\Delta\theta_{peak}$) were determined for the three crosswind velocities at the reference fan operating conditions and near-stall (Fig. 11 and Fig. 12). These are defined as the values above the single-passage configuration at near stall conditions (Fig. 11). For the crosswind configurations with attached flow at the intake ($V_{CW} = V_{CW}^{ref} - 5kts$ and $V_{CW} = V_{CW}^{ref}$), the exposure to incidence distortion increases up to values of $\theta/\theta_{bp} = 7$ to 8 at near stall conditions, with similar values of Δi^{peak} ($\Delta i^{peak} \approx 20^o$). However, the grossly separated intake case ($V_{CW} = V_{CW}^{ref} - 5kts$) reaches values of $\Delta i^{peak} = 47^o$ and exposures up to $\theta/\theta_{bp} = 14$, also at near-stall conditions. For the three crosswind configurations, $\Delta\theta_{peak}/\theta_{bp}$ increases by more than $2\theta_{bp}$ from the reference fan operation to near-stall, with values above $\Delta_{peak}\theta/\theta_{bp} > 7$. Therefore, for the three crosswind conditions, the azimuthal exposure to peak distortion increases by more than $2\theta_{bp}$ between the reference Q_{fan} and near stall operations. This is consistent with the literature [20, 25]. Stall cells are formed at regions of high blade incidence but these only grow when the circumferential extent of incidence distortion is sufficient to sustain the disturbances across several revolutions [20, 25].

3.4 Effect of intake distortion on fan stall onset

The onset of spike-type fan stall for the $V_{CW} = V_{CW}^{ref} - 5kts$ configuration is affected by the variations in the intake flow. On the windward side ($\theta/\theta_{bp} = 0 - 7.5$, Fig 10), the fan operates within a region affected by fan-induced local separation regions and secondary flows due to the counter-rotating ground vortex. This leads to a reduction in flow coefficient which increases the blade incidence angle and reduces relative Mach number. As the fan tip progresses azimuthally from $\theta/\theta_{bp} = 7.5 - 9$, it encounters the counter-rotating ground vortex which increases the tangential velocity and consequently the blade incidence angle. The increase in blade incidence angle causes local flow separation at the fan passage (Fig. 13b), which increases flow blockage and affects subsequent blades [20]. Consequently, a stall cell forms downstream of the ground-vortex region and propagates azimuthally around

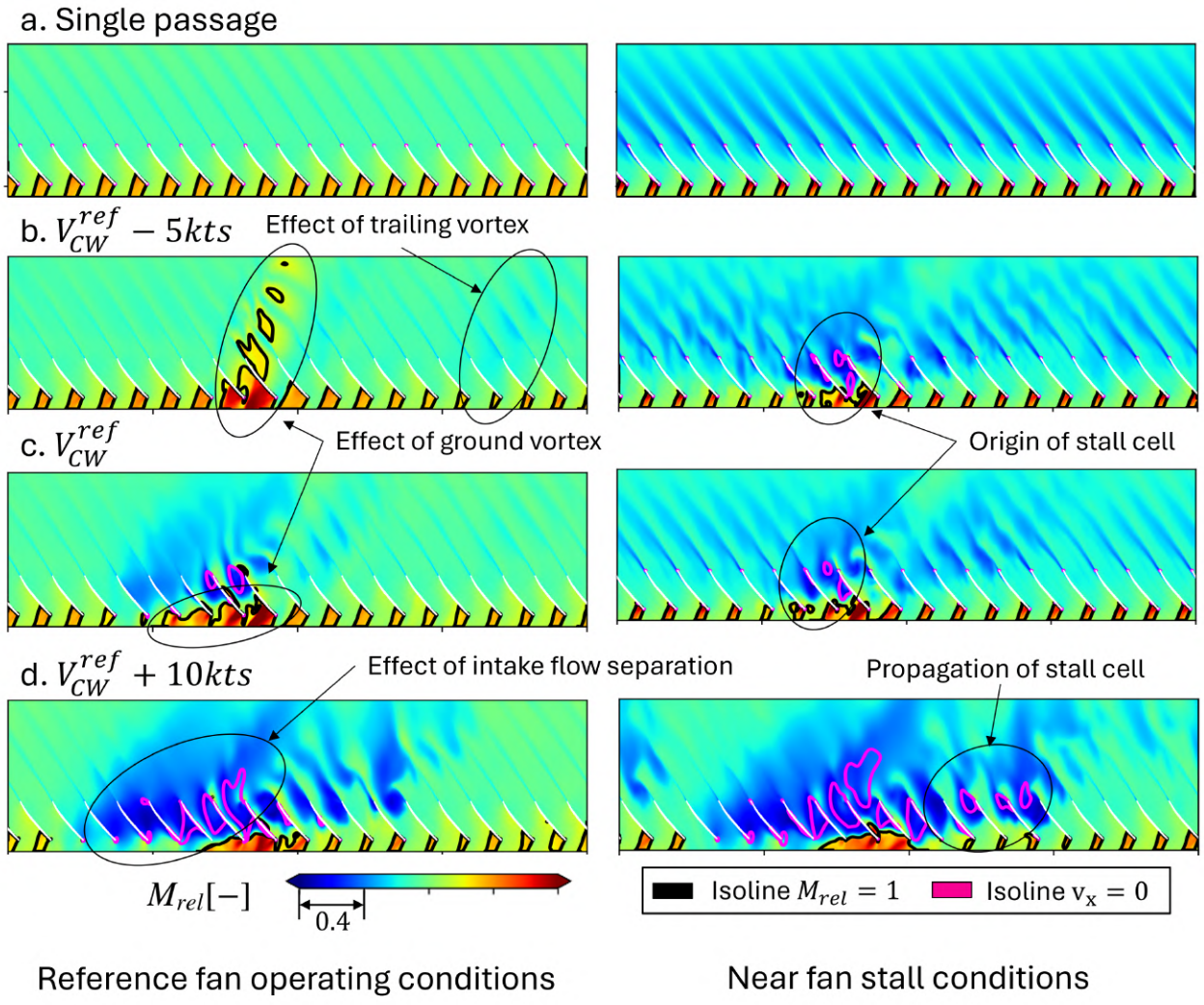


Figure 13 – Relative Mach (M_{rel}) distributions at circumferential plane across the fan ($r/R_{fan} = 0.95$). The figure includes (a) the steady RANS single passage solutions and snapshots for the cases at (b) $V_{CW} = V_{CW}^{ref} - 5kts$, (c) $V_{CW} = V_{CW}^{ref}$ and (c) $V_{CW} = V_{CW}^{ref} + 10kts$. The figure includes isolines of $M_{rel} = 1$ and of axial velocity $v_x = 0$.

the annulus (Fig. 9a and 13b). This cell periodically engages with the distorted flow field and develops into rotating stall (Fig. 9a). This can be seen in the time-space diagram where the disturbance in static pressure at the casing originates right after the ground vortex region ($\theta/\theta_{bp} = 7.5 - 9$, Fig. 9a) and at the circumferential plane across the fan (Fig. 13b). The fan stall onset is similar for the crosswind case at $V_{CW} = V_{CW}^{ref}$. At these conditions, the intake aerodynamics at near-stall Q_{fan} is similar to $V_{CW} = V_{CW}^{ref}$ (Fig. 13b). For the grossly separated intake flow conditions ($V_{CW} = V_{CW}^{ref} + 10kts$), the disturbance in casing static pressure originates in the region of grossly separated flow (Fig. 9b and 13c). However, this disturbance initially does not grow at near-stall conditions. At the fan stall point, the ground vortex and related secondary flows enlarge the azimuthal extent of peak distortion which develops the disturbance into a rotating stall cell. Therefore, although the intake aerodynamics at near-stall conditions is substantially different relative to the cases at lower crosswind velocities, there are some similarities in the onset of fan stall.

In conclusion, it has been found that the fan spike-type stall onset process for counter-rotating ground vortex arrangements is similar for the three crosswind conditions investigated: local flow separations within the fan passage originate in regions with increased blade incidence angle associated with flow separation or ground vortex. This increases flow blockage, propagates to nearby passages

and generates a spike disturbance. At near stall conditions the flow becomes more unsteady with fluctuations in blade incidence angle which lead to increased azimuthal exposures to peak incidence distortion. This develops the disturbance into a rotating stall cell across multiple fan revolutions. These results are consistent with the findings in the literature where clean flow and distorted flow configurations followed the same stall inception process with the main difference being the stall margin [8].

4. Conclusions

This work presents an analysis of the effects of intake flow distortion on the fan performance and onset of rotating stall. A podded, short intake coupled with a fan under crosswind conditions was assessed with unsteady CFD in a wind tunnel arrangement. The fan was driven to stall under three counter-rotating crosswind conditions that encompassed attached, transitional and grossly separated intake flow regimes from the reference fan operating conditions to rotating stall.

For the cases at low and reference crosswind velocities, the intake flow was predominantly attached at near fan stall conditions. For these cases, flow distortion was associated with the ground vortex, bulk swirl, fan-induced local separation regions and secondary flows induced by the ground vortex. These led to a stall margin loss of up to 5% relative to the single-passage baseline configuration. At the highest crosswind velocity, the intake flow was grossly separated across the full operating range due to shock-induced lip separation. This resulted in significantly higher levels of total pressure and swirl distortion and unsteadiness at the fan inlet which led to a notable reduction of fan stall margin with a reduction of up to 11.6% relative to the clean flow configuration.

An analysis of the intake aerodynamics in the relative frame of reference at near-stall conditions indicates that, there are some similarities in the flow distortion characteristics and the onset of spike-stall for all crosswind velocities. In all cases for this counter-rotating arrangement, the fan blades first encounter regions of reduced flow coefficient associated with intake diffusion or flow separation, combined with secondary flows related to the ground vortex. After these, the blades encounter a counter-rotating ground vortex which also increases blade incidence. These lead to flow separation within the fan passage, which increases flow blockage, affects subsequent blades and generates a disturbance. As fan stall conditions are approached, increased unsteadiness in blade incidence angle extends the azimuthal exposure to adverse conditions which promotes the development of the disturbance into a rotating stall cell.

Overall, these results demonstrate that while the process by which rotating stall is initiated is similar for the three crosswind conditions, the intake aerodynamic state influences the fan operating margin at which stall occurs. These findings underline the importance of capturing intake–fan aerodynamic coupling and realistic crosswind distortion characteristics in the assessment and design of the next generation of propulsion systems.

5. Acknowledgments

This work was partially funded by Cranfield University, Rolls-Royce plc. and the Innovate UK AZTEC project (10126421).

6. Contact Author Email Address

mailto: j.hueso-rebassa@cranfield.ac.uk

7. Copyright Statement

The authors confirm that they, and/or their company or organization, hold copyright on all of the original material included in this paper. The authors also confirm that they have obtained permission, from the copyright holder of any third party material included in this paper, to publish it as part of their paper. The authors confirm that they give permission, or have obtained permission from the copyright holder of this paper, for the publication and distribution of this paper as part of the ICAS proceedings or as individual off-prints from the proceedings.

8. Data availability

Due to commercial confidentiality agreements the supporting data is not available.

References

[1] L. Boscagli, D. MacManus, R. Christie, and C. Sheaf. Effect of unsteady fan-intake interaction on short intake design. *Journal of Engineering for Gas Turbines and Power*, 146, 3 2024.

[2] N. T. Brich. 2020 Vision: The Prospects for Large Civil Aircraft Propulsion. *The Aeronautical Journal*, 104(1038):347–352, 2000.

[3] F. Haselbach. Next generation of large civil aircraft engines-concepts & technologies. In *11 European Conference on Turbomachinery Fluid dynamics & Thermodynamics*, Madrid, Spain, 2015.

[4] T. Cao, N. R. Vadlamani, P. G. Tucker, A. R. Smith, M. Slaby, and C. Sheaf. Fan-intake interaction under high incidence. In *Proceedings of ASME Turbo Expo 2021 - GT2016-56566*, 6 2016.

[5] W. T. Cousins. History, philosophy, physics, and future directions of aircraft propulsion system/inlet integration. In *Volume 2: Turbo Expo 2004*, pages 305–320. ASMEDC, 1 2004.

[6] L. Boscagli, R. Christie, D. MacManus, and T. Piovesan. Aerodynamics of a short intake in crosswind. *Aerospace Science and Technology*, 129:107826, 10 2022.

[7] W. Zhang and M. Vahdati. A parametric study of the effects of inlet distortion on fan aerodynamic stability. *Journal of Turbomachinery*, 141, 1 2019.

[8] A. Awes, A. Brosse, G. Dufour, X. Carbonneau, and B. Godard. Effect of a vortex distortion on the operability of an ultra high bypass ratio fan. In *Proceedings of ASME Turbo Expo 2020 - GT2020-14596*, 9 2020.

[9] T. Piovesan, P. K. Zachos, D. G. MacManus, and C. Sheaf. Unsteady swirl distortion in a short intake under crosswind conditions. *AIAA Journal*, 63:1867–1884, 5 2025.

[10] J. Hueso-Rebassa, D. MacManus, F. Tejero, T. Williams, Y. Frey, and G. Thorne. Characterisation of aerodynamics and flow distortion on a short intake coupled with a fan in crosswind. In *Proceedings of ASME Turbo Expo 2026 - GT2026-176526*, 6 2026.

[11] J. P. Murphy and D. G. MacManus. Intake ground vortex prediction methods. *Journal of Aircraft*, 48:23–33, 1 2011.

[12] A. N. Rao, P. Sureshkumar, S. Stapelfeldt, B. Lad, K. Lee, and R. P. Rico. Unsteady analysis of aeroengine intake distortion mechanisms: Vortex dynamics in crosswind conditions. *Journal of Engineering for Gas Turbines and Power*, 144, 12 2022.

[13] L. Lobuono, D. MacManus, and R. Christie. Effect of intake length on flow interactions in a coupled compact intake-fan in crosswind. In *AIAA Aviation Forum and Ascend 2025*. American Institute of Aeronautics and Astronautics, 7 2025.

[14] A. Castillo Pardo, E. Gunn, T. S. Williams, C. Hall, T. Brandvik, and S. Baralon. Crosswind aerodynamics of low pressure ratio fans. *Journal of the Global Power and Propulsion Society*, 9:143–159, 2025.

[15] N. R. Vadlamani, T. Cao, R. Watson, and P. G. Tucker. Toward future installations: Mutual interactions of short intakes with modern high bypass fans. *Journal of Turbomachinery*, 141, 8 2019.

[16] E. J. Gunn, T. Brandvik, and M. J. Wilson. Fan-intake coupling with conventional and short intakes. In *Proceedings of ASME Turbo Expo 2021 - GT2021-58829*, 6 2021.

[17] L. Lobuono, D. MacManus, J. Hueso-Rebassa, and R. Christie. Unsteady flow interactions and ground plane proximity in a coupled compact intake-fan in crosswind. In *34th Congress of the International Council of the Aeronautical Sciences - Paper 263*, pages 24–26, 9 2025.

[18] M. Migliorini, P. K. Zachos, and D. G. MacManus. Novel method for evaluating intake unsteady flow distortion. *Journal of Propulsion and Power*, pages 1–13, September 2021.

[19] D. Perovic, C. A. Hall, and E. J. Gunn. Stall inception in a boundary layer ingesting fan. *Journal of Turbomachinery*, 141, 9 2019.

[20] G. Pullan, A. M. Young, I. J. Day, E. M. Greitzer, and Z. S. Spakovszky. Origins and structure of spike-type rotating stall. *Journal of Turbomachinery*, 137, 5 2015.

[21] N. M. McDougall, N. A. Cumpsty, and T. P. Hynes. Stall inception in axial compressors. *Journal of Turbomachinery*, 112:116–123, 1 1990.

[22] M. Hewkin-Smith, G. Pullan, S. D. Grimshaw, E. M. Greitzer, and Z. S. Spakovszky. The role of tip leakage flow in spike-type rotating stall inception. *Journal of Turbomachinery*, 141, 6 2019.

[23] A. Thiam, R. Whittlesey, C. Wark, and D. Williams. Corner separation and the on-set of stall in an axial compressor. In *38th Fluid Dynamics Conference and Exhibit*. American Institute of Aeronautics and Astronautics, 6 2008.

[24] S. Weichert and I. Day. Detailed measurements of spike formation in an axial compressor. *Journal of Turbomachinery*, 136, 5 2014.

[25] O. Allen, A. Castillo Pardo, and C. A. Hall. An experimental investigation into the impacts of varying the circumferential extent of tip-low total pressure distortion on fan stability. In *Proceedings of ASME Turbo Expo 2021 - GT2021-59851*, 6 2021.

[26] T. Williams, C. Hall, and M. Wilson. Low pressure ratio transonic fan stall with radial distortion. *Journal of the Global Power and Propulsion Society*, 4:226–237, 12 2020.

[27] F. Tejero, D. MacManus, J. Hueso-Rebassa, Y. Frey-Marioni, and I. Bousfield. Aerodynamics of a short intake at high incidence. In *Proceedings of the 16th Turbomachinery Conference (ETC16) - ETC2025-298*, 3 2025.

[28] P. Moinier. *Algorithm Developments for an Unstructured Viscous Flow Solver*. PhD thesis, University of Oxford, 1999.

[29] F. R. Menter. Two-Equation Eddy-Viscosity Turbulence Models for Engineering Applications. *AIAA Journal*, 32(8):1598–1605, 1994.

[30] P. I. Crumpton, P. Moinier, and M. B. Giles. An Unstructured Algorithm for High Reynolds Number Flows on Highly Stretched Grids. In *Proceedings of the 10th International Conference on Numerical Methods for Fluid Dynamics*, 1997.

[31] C. Misev and N. J. Hills. Steepest Descent Optimisation of Runge–Kutta Coefficients for Second Order Implicit Finite Volume CFD Codes. *Journal of Computational Physics*, 354:576–592, 2018.

[32] W. Sutherland. The Viscosity of Gases and Molecur Force. *Philosophical Magazine*, 5(35):507–531, 1893.

[33] D. Amirante, V. Ganine, N. Hills, J. Nicholas, and P. Adami. A Coupling Framework for Multi-Domain Modelling and Multi-Physics Simulations. *Entropy*, 23(6), 2021.

[34] V. Ganine, D. Amirante, and N. Hills. Enhancing Performance and Scalability of Data Transfer Across Sliding Grid Interfaces for Time-Accurate Unsteady Simulations of Multistage Turbomachinery Flows. *Computers & Fluids*, 115:140–153, 2015.

[35] Siemens Digital Industries Software. Simcenter STAR-CCM+ User Guide v. 2023.4, Siemens 2023.

[36] SAE International. ARP1420: Gas turbine engine inlet flow distortion guidelines, 2017.

[37] J. Seddon and E. L. Goldsmith. *Intake Aerodynamics*. Blackwell, 1999.

[38] B. Mohankumar, C. Hall, and M .Wilson. Fan Aerodynamics With a Short Intake at High Angle of Attack. *Journal of Turbomachinery*, 143(5):051003, 2021.